Energy Conversion and Management: X 31 (2026) 101963

Contents lists available at ScienceDirect

Energy Conversion and Management: X

journal homepage: www.sciencedirect.com/journal/energy-conversion-and-management-x

# Receding-horizon optimal control of tidal barrage power plants: Impact of weather dependent tidal variations

Agustina Skiarski [a], [*], Nicolás Faedo [b], John V. Ringwood [a]

[a] Centre for Ocean Energy Research, Department of Electronic Engineering, Maynooth University, Maynooth, Co. Kildare, Ireland
[b] Marine Offshore Renewable Energy Lab, Department of Mechanical and Aerospace Engineering, Politecnico di Torino, Torino, Italy

## ARTICLE INFO

*Keywords:*
Tidal barrages
Optimal control
Storm surge
Receding-horizon control
Ocean energy

## ABSTRACT

Tidal barrage power plants leverage the daily variations in sea water level to generate electricity. Optimising tidal barrage operation requires the solution of an associated continuous-time optimal control problem, by looking at the past tidal elevation, as well as the predicted tidal elevation during subsequent tidal cycles. Although highly predictable, the tidal level variations are also influenced by stochastic weather conditions, which are often neglected when assessing tidal barrage energy generation. In this study, a receding-horizon control framework is proposed, whereby optimal operation of tidal barrages can be computed, while including both past observations of the tidal elevation, as well as a tidal level forecast, based either on weather data or on the astronomic tide alone. At each step of the receding-horizon algorithm, tidal barrage optimal operation is computed using moment-based control, a mathematical method that enables the transcription of the infinite-dimensional tidal barrage optimal control problem onto a finite dimensional nonlinear programme. With this framework, the impact of considering the storm surge within the control calculations, as opposed to only considering astronomic tidal forcing, is assessed. Including a state-of-the-art weather-informed forecast, as opposed to a purely astronomic forecast, in the representation of the tidal elevation is shown to improve the performance of the controller, highlighting the value of accounting for the storm surge when computing tidal barrage optimal operation.

## 1. Introduction

Deployment of renewable power plants is key to decreasing greenhouse gas emissions and sustainably tackling climate change. Among the different renewable energy sources available, the tidal range, *i.e.* the difference between high and low sea water level, is slowly varying, and highly predictable, since the bulk of tidal forcing is originated by interactions between the Earth and the Moon, and between the Earth and the Sun. The potential energy from the tidal range can be harnessed by tidal barrage power plants. Fig. 1 shows a schematic representation of a tidal barrage, where an embankment, with turbines and sluice gates, is placed in a coast or estuary, separating a basin from the open sea. As the tidal level rises and falls, the difference in water level inside and outside the basin drives water through the turbines, generating mechanical power. This mechanical power is subsequently converted into electrical power by electrical generators, coupled to the turbines. The sluice gates, placed along the barrage wall, add flexibility to the barrage operation by increasing the flow through the barrage, without power conversion. Additionally, turbines can be operated to pump water into and out of the basin during certain periods, increasing available potential energy, and subsequent power generation. Examples of large-scale operating tidal barrages are La Rance, in the north of France, and Sihwa Lake, in South Korea; on the other hand, several projects have been proposed along the coast of the UK [1], where the tidal range is one of the highest around the world.

In tidal barrages, turbine generation is a function of the turbine flow, $Q_t$, and the head $H$, *i.e.* the difference between the inner basin level, $n_i$, and the outer sea level, $n_o$. $n_i$ depends on previous operation of the barrage, *i.e.* how much the basin has been previously filled or emptied, subsequently affecting $H$; moreover, turbine flow $Q_t$, at a certain time, not only determines instantaneous power generation, but also conditions the future available head $H$, that is, how much power can be generated during subsequent cycles. Hence, optimising tidal barrage operation should be formulated as an optimal control problem (OCP) during a time window, where past and future tidal cycles are included, which suggests the need for a tidal level forecast.

As a first step, the tidal elevation at a particular location can be approximated by the sum of astronomic constituents, which are harmonic functions, each representing different periodic astronomical

---

[*] Corresponding author.
*E-mail address:* agustina.skiarski.2024@mumail.ie (A. Skiarski).

https://doi.org/10.1016/j.ecmx.2026.101963
Received 16 March 2026; Received in revised form 6 May 2026; Accepted 12 May 2026

## Nomenclature

| | |
|---|---|
| $\mathcal{A}$ | Extended vector of collocated time instants |
| $A_b$ | Basin wetted surface area [m$^2$] |
| $A_s$ | Sluice gate area [m$^2$] |
| $A_s^{n_a}$ | Sluice gate area solution using $n_a$ as prediction [m$^2$] |
| $A_s^{n_f}$ | Sluice gate area solution using $n_f$ as prediction [m$^2$] |
| $A_s^{n_o}$ | Sluice gate area solution using $n_o$ as prediction [m$^2$] |
| $\mathcal{B}_{n_i}$ | Matrix of collocated state constraint |
| $\mathcal{B}_{\mathbf{u}}$ | Matrix of collocated input constraints |
| $\mathcal{B}_{P_t}$ | Matrix of collocated power constraint |
| $C_{ds}$ | Sluice gate discharge coefficient |
| $d$ | Number of harmonics |
| $\Delta_E$ | Energy difference [GWh] |
| $\Delta_{n_i}$ | Cumulative state constraint deviation [m] |
| $E$ | Tidal barrage generated energy [GWh] |
| $E^{n_a}$ | Energy generated using $n_a$ as prediction [GWh] |
| $E^{n_f}$ | Energy generated using $n_f$ as prediction [GWh] |
| $E^{n_o}$ | Energy generated using $n_o$ as prediction [GWh] |
| $g$ | Gravitational acceleration [m/s$^2$] |
| $\mathcal{G}$ | Moment-based signal generator |
| $H$ | Hydraulic head [m] |
| $\mathcal{J}$ | Control objective function |
| $L_{A_s}$ | Moment-domain projection of $A_s$ |
| $\mathcal{L}^N$ | Windowing mapping |
| $L_{n_e}$ | Moment-domain projection of $n_e$ |
| $L_{n_i}$ | Moment-domain projection of $n_i$ |
| $L_{Q_t}$ | Moment-domain projection of $Q_t$ |
| $L_{\mathbf{u}}$ | Moment-domain projection of $\mathbf{u}$ |
| $\Lambda$ | Vector of collocated time instants |
| $M_2$ | Lunar semidiurnal astronomic constituent |
| $\mu$ | Turbine efficiency |
| $N$ | Receding-horizon step |
| $N^{\max}$ | Maximum receding-horizon step |
| $n_a$ | Astronomic tidal elevation [m] |
| $N_c$ | Time collocation points |
| $n_e$ | Controller representation of tidal elevation [m] |
| $n_i$ | Inner basin level [m] |
| $n_i^{\max}$ | Maximum inner basin level [m] |
| $n_i^{\min}$ | Minimum inner basin level [m] |
| $n_f$ | Weather-informed tidal forecast [m] |
| $n_o$ | Sea water level [m] |
| $n_s$ | Storm surge [m] |
| $n_t$ | Number of tidal barrage turbines |
| $N_t$ | Number of time steps |
| $\nu$ | Dimension of signal generator |
| $P_t$ | Tidal barrage generated power [MW] |
| $P_t^{\max}$ | Maximum tidal barrage power [MW] |
| $\Phi$ | Horizon period [h] |
| $\Phi_c$ | Control period [h] |
| $\Phi_f$ | Future time period [h] |
| $\Phi_p$ | Past time period [h] |
| $\Phi_t$ | Transition period [h] |
| $Q_t$ | Turbine flow [m$^3$/s] |
| $Q_t^{n_a}$ | Turbine flow solution using $n_a$ as prediction [m$^3$/s] |
| $Q_t^{n_f}$ | Turbine flow solution using $n_f$ as prediction [m$^3$/s] |
| $Q_t^{n_o}$ | Turbine flow solution using $n_o$ as prediction [m$^3$/s] |
| $Q_s$ | Sluice gate flow [m$^3$/s] |
| $\theta$ | Vector of basis functions |
| $R$ | Time-collocated residual function |
| $\mathcal{R}$ | Residual function |
| $\rho$ | Density of the sea water [kg/m$^3$] |
| $S$ | Dynamic matrix of signal generator |
| $T_c$ | Control time [h] |
| $T_h$ | Time horizon [h] |
| $t_N$ | Current time instant [h] |
| $T_t$ | Transition time [h] |
| $\mathbf{u}$ | Vector of optimisation variables |
| $\mathbf{u}^{\max}$ | Maximum constraint of optimisation variables |
| $\mathbf{u}^{\min}$ | Minimum constraint of optimisation variables |
| $\omega_{co}$ | Cutoff frequency [rad/h] |
| $\omega_{M_2}$ | Lunar semidiurnal frequency [rad/h] |
| $\omega_o$ | Fundamental frequency [rad/h] |
| $\Omega$ | Total simulation time [h] |
| $\xi$ | Transition function |

forcing:

$$n_a(t) = \sum_c A_c \cos(\omega_c t + \phi_c), \tag{1}$$

where $n_a(t)$ is the *astronomic tidal elevation*, and each $c$ constituent is associated with an amplitude $A_c$, a frequency $\omega_c$ and a phase $\phi_c$. The astronomic tide is highly predictable in advance, given the knowledge of the trajectory of celestial bodies, and is often an accurate representation of the real tidal elevation. In most sites around the globe, the most predominant tidal constituent is the $M_2$ constituent, associated with the gravitational interaction between the Earth and the Moon [2]. However, the tidal elevation can also be affected by weather conditions, such as wind speed and direction, and atmospheric pressure. The tidal variations caused by changes in wind and pressure are often referred to as storm surge [2], and are more difficult to forecast, compared to astronomic tides.

The tidal barrage OCP has been address in the literature by either implementing standard discretisation techniques, such as Model Predictive Control (MPC) [3], or separating the barrage operation into distinct modes (generating, sluicing and pumping) and optimising their duration [4,5]. In particular, moment-based control was recently implemented in tidal barrage optimisation to discretise the OCP in the frequency domain [6], using a family of harmonic basis functions, similar to spectral and pseudo-spectral methods, with the advantage of guaranteeing existence and uniqueness of the control solution [7]. In the literature on tidal barrage operation, the tidal elevation is assumed to be known in advance, and is typically modelled using astronomic constituents [8]. [9] studies the impact of storm surge on the power output of proposed tidal barrages around the coast of the UK, assuming pre-defined barrage operation, without optimisation involved. To the best of the authors' knowledge, there are no studies that analyse how tidal barrage optimal *operation* changes when considering storm surge.

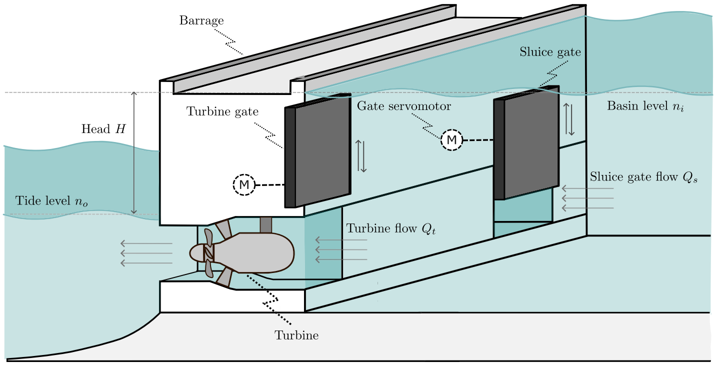

**Fig. 1.** Diagram of a tidal barrage power plant [6].

**Table 1**
Parameterisation of the La Rance power plant model, from [10].

| Parameter | Value | Unit |
|---|---|---|
| Maximum sluice gate area $A_s^{\max}$ | 900 | m$^2$ |
| Number of turbines $n_t$ | 24 | – |
| Turbine rated power | 10 | MW |
| Maximum turbine flow $Q_t^{\max}$ | 260 | m$^3$/s |
| Sluice discharge coefficient $C_{ds}$ | 1 | – |

This study presents a nonlinear receding-horizon optimal control framework, whereby real (past) tidal elevation observations, as well as a tidal elevation forecast at the prediction horizon, can be included within the tidal barrage control calculations. The novelty of the work relies on the implementation of a receding-horizon control algorithm together with moment-based optimal control, in the particular case of tidal barrage operation, whereby the impact of neglecting storm surge within the OCP can be studied, by using different tidal elevation forecasts. Prior work on tidal barrage optimisation use the astronomic tide as input, which is available at any time in the future; here, the receding-horizon framework is used to effectively include a storm surge forecast within the control calculations, which is available only in a receding-horizon basis, that is, for a limited time period. While previous MPC approaches, applied to tidal barrage optimisation, discretise the OCP in time, in this study, moment-based control is used to discretise the tidal barrage OCP and compute the optimal trajectories of turbine and sluice gate flows at each step of the receding-horizon algorithm.

The reminder of this paper is organised as follows: Section 2 describes the tidal barrage model, used in this study for the control calculations, and Section 3 presents the receding-horizon moment-based control framework. Section 4 presents the results obtained from using different tidal forecasts, and the conclusions are outlined in Section 6.

## 2. Tidal barrage model

In this section, the tidal barrage model, used in this study to formulate and solve the associated tidal barrage OCP, is described. The case study presented is based on the La Rance power plant, located in St. Malo, France. Table 1 shows the design parameters of the La Rance power plant [10] considered in this study.

### 2.1. Tidal elevation

As mentioned in Section 1, the tidal elevation $n_o(t)$ can be modelled as:

$$n_o(t) = n_a(t) + n_s(t), \tag{2}$$

where $n_a(t)$ the astronomic tide, and $n_s(t)$ is the storm surge. In this study, the (observed) tidal elevation $n_o(t)$ is obtained from tidal gauge observations at the St. Malo tidal gauge station [11], where the La Rance power plant is located. The astronomic tide $n_a(t)$ is extracted from the EOT20 global tidal model [12], which provides the amplitude and phase of 17 harmonic constituents present in the astronomic tides, for a particular location. As a result, the storm surge $n_s(t)$ at La Rance can be approximated, as per Eq. (2), as the difference between $n_o(t)$ and $n_a(t)$. Fig. 2 shows a histogram of the storm surge in St. Malo, using data from 2020 to 2024. At this location, the storm surge is mostly between −1 m and 1 m, and does not present strong seasonality. Note that the tidal range in St. Malo is between 9 m and 14 m [13]; therefore, the storm surge component, on average, accounts for approximately between 7% and 11% of the tidal range.

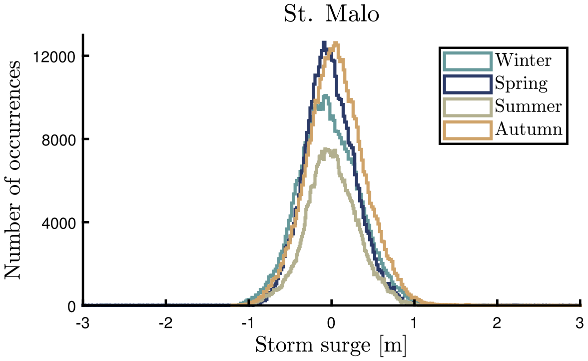

**Fig. 2.** Distribution of storm surge driven tidal level in St. Malo.
*Source:* Data from 2020 to 2024.

Fig. 3(a) shows the observed tidal height against the astronomic tide and weather-informed forecast, while Fig. 3(b) shows the real storm surge, as per Eq. (2), and the storm surge predicted from the weather-informed forecast, *i.e.* $n_f - n_a$. The tidal elevation at La Rance, during the period under consideration, has a maximum range of approximately 13 m, and a maximum absolute surge of 1 m, that is, around 8% of the tidal range. While the root mean squared error (RMSE) between $n_o$ and $n_a$ is 0.35 m, the RMSE between $n_o$ and $n_f$ is 0.15 m.

### 2.2. Governing equations

The turbines and sluice gates, placed along the barrage wall, allow the passage of water into and out of the basin, which determines the water level inside the basin, $n_i(t)$. In the case of the turbines, the flow $Q_t(t)$ can be controlled by manipulating the guide vanes and runner blades in the turbine, and hydraulic power is converted to mechanical power, $P_t(t)$, as per the following equation:

$$P_t(t) = \rho g \mu(Q_t, H) Q_t(t) H(t), \tag{3}$$

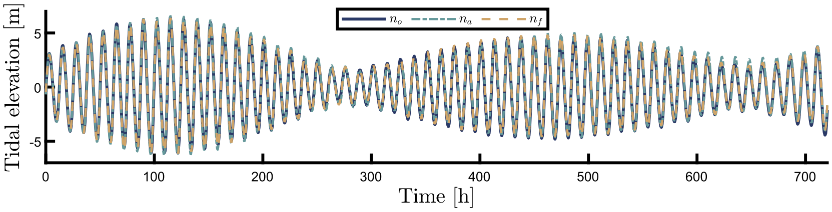

(a) Observed (measured) tidal elevation $n_o$, astronomic tidal forecast $n_a$, and weather-informed forecast $n_f$, used as external inputs within the controller.

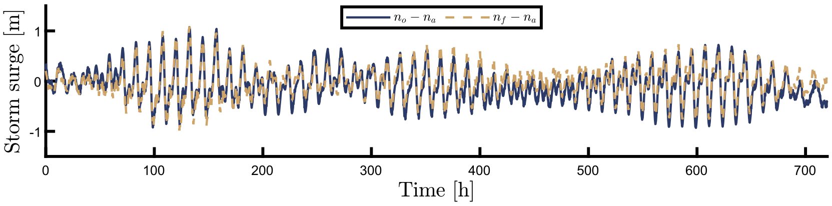

(b) Real storm surge $n_o - n_a$, and storm surge from weather-informed tidal forecast $n_f - n_a$.

**Fig. 3.** Tidal elevation data from St. Malo.

where $\rho$ is the water density, $g$ is the gravitational acceleration, and $\mu(Q_t, H)$ is the turbine efficiency, which is a function of $Q_t$ and $H$. A detailed description of the turbine efficiency model can be found in [6]. On the other hand, the water flows through the sluice gates driven purely by gravity, without energy conversion, controlled by the total sluice gate opening area $A_s(t)$:

$$Q_s(t) = \mathrm{sign}(H(t)) C_{ds} A_s(t) \sqrt{2\ g|H(t)|}, \tag{4}$$

where $C_{ds}$ is the discharge coefficient. Using a simplifying 0-D hydrodynamic model [14], the inner basin level $n_i(t)$ varies proportionally with the total flow through the barrage:

$$\dot{n}_i(t) = \frac{-Q_t(t) - Q_s(t)}{A_b(n_i)} = f(n_i, n_o, Q_t, A_s), \tag{5}$$

$A_b(n_i)$ being the basin area, which can be modelled as a function of $n_i$, to account for the bathymetry of the site. In this study, it is assumed that $A_b$ is a linear function of $n_i$, which has been validated in [10] using real data from the La Rance power plant. Note that the 0-D hydrodynamic model, together with the linear function $A_b(n_i)$, are sources of error within the optimal control calculations, but with the advantage of being numerically tractable; using higher dimensional hydrodynamic models, while being more accurate, significantly increase the dimensionality of the barrage system model.

## 3. Optimal control formulation

In this section, the receding-horizon moment-based controller, used in this study to compute tidal barrage optimal operation, is presented. Assuming that the objective is to maximise energy generation during a period $\Phi = [0, T_h] \subset \mathbb{R}^+$, the constrained nonlinear tidal barrage OCP can be formulated as[1]:

$$\mathbf{u}^{\mathrm{opt}} = \arg\max_{\mathbf{u}} \int_{\Phi} P_t(n_i, n_o, \mathbf{u}) \mathrm{d}t,$$

subject to:

$$\begin{aligned} &\dot{n}_i = f(n_i, n_o, \mathbf{u}), \\ &n_i^{\min} \le n_i \le n_i^{\max}, \\ &\mathbf{u}^{\min} \le \mathbf{u} \le \mathbf{u}^{\max}, \\ &P_t \le P_t^{\max}, \end{aligned} \tag{6}$$

where $n_i$ is the state of the system, $n_o$ the external input (*i.e.* the tidal elevation), and $\mathbf{u} = [Q_t, A_s]$ is the vector of controlled variables.

Tidal barrage power plants harness the energy from tidal level variations which, as described in Section 2, have a predominantly harmonic behaviour; hence, the dominant dynamics of the tidal barrage system are given by the periodic changes in tidal level. As such, it is reasonable to approximate the tidal elevation, as well as the barrage system controls and state variables, using harmonic functions. In moment-based control, an OCP can be parameterised with a family of (trigonometric) basis functions, generated by a dynamic *signal generator*, and the steady-state response of the system can be approximated by using the mathematical notion of *moments*. If the problem is well-posed, the approximated solution in the moment domain is guaranteed to converge to the steady-state response of the system [15]. The interested reader is referred to [6,16] for further insights on moment-based control applied to tidal barrages.

### 3.1. Moment-based control of tidal barrages

This paper uses a moment-based control framework to transcribe the infinite-dimensional OCP of tidal barrage operation into a finite-dimensional nonlinear programme, following the procedure described, in detail, in [6]. To keep the manuscript relatively self-contained, in this section, the mathematical formulation of tidal barrages moment-based parameterisation is briefly recalled.

Considering the state equation describing the single-input-single-output (SISO) nonlinear tidal barrage system $f : \mathbb{R} \times \mathbb{R} \times \mathbb{R}^2 \to \mathbb{R}$ (by replacing Eq. (4) in Eq. (5)):

$$\dot{n}_i = \frac{-Q_t - \mathrm{sign}(n_i - n_o) C_{ds} A_s \sqrt{2\ g|n_i - n_o|}}{A_b(n_i)} = f(n_i, n_o, \mathbf{u}). \tag{7}$$

Leveraging the predominantly harmonic behaviour of the tidal elevation, driven by astronomical forcing, the following harmonic signal generator $\mathcal{G}$ is formulated:

$$\mathcal{G} : \begin{cases} \dot{\theta} = S\theta, \\ n_o \approx n_e = L_{n_e}\theta, \end{cases} \tag{8}$$

with

$$\theta = \begin{bmatrix} 1 \\ \cos \omega_o t \\ \sin \omega_o t \\ \dots \\ \cos d\omega_o t \\ \sin d\omega_o t \end{bmatrix}, \quad S = 0 \oplus \left( \bigoplus_{p=1}^{d} \begin{bmatrix} 0 & p\omega_o \\ -p\omega_o & 0 \end{bmatrix} \right), \tag{9}$$

---

[1] From this point forward, the time dependence of the variables is omitted when clear from the context.

where $\theta \in \mathbb{R}^{\nu}$, $S \in \mathbb{R}^{\nu\times\nu}$, with $\nu = 2d + 1$, and $n_e$ is the description of the real tidal elevation, $n_o$, within the controller. $L_{n_e}^{\top} \in \mathbb{R}^{\nu}$ is a vector of coefficients that projects $n_e$ onto $\theta$; that is, the tidal elevation $n_o$ is approximated as a linear combination of a harmonic subspace, with fundamental frequency $\omega_o$, and $d$ the number of harmonics. The fundamental frequency depends on $T_h$, the length of the time period considered for the control calculations, *i.e.* $\omega_o = 2\pi/T_h$; that is, the discretisation of the problem depends on the choice of $T_h$, which is discussed in Section 4.1. For a fixed cutoff frequency $\omega_{co}$, the number of harmonics present in the signal generator $\mathcal{G}$ is $d = \text{floor}\left(\frac{\omega_{co}}{\omega_o}\right)$. In the particular case of tidal barrage optimal control, it was found that $\omega_{co}$ should be at least 20 cycles/day [6]; in this study, a value of $\omega_{co} = 28$ cycles/day is chosen.

Suppose now that the control variables, represented by the vector $\mathbf{u}= [Q_t, A_s]$, can also be approximated with harmonic functions, assuming that the astronomic tide dictates the dominant system dynamics. Then, the control variables are parameterised as a linear combination of the basis functions in $\theta$:

$$\mathbf{u}= \begin{bmatrix} Q_t \\ A_s \end{bmatrix} = \begin{bmatrix} L_{Q_t} \\ L_{A_s} \end{bmatrix} \theta = L_{\mathbf{u}}\theta, \tag{10}$$

where $L_{\mathbf{u}}^{\top} = [L_{Q_t}^{\top} \, L_{A_s}^{\top}] \in \mathbb{R}^{\nu\times 2}$ is the vector defining the projection of $Q_t$ and $A_s$ in the moment domain. The resulting interconnected system has the form

$$\begin{aligned} \dot{\theta} &= S\theta, \\ \dot{n}_i &= f(n_i, L_{n_e}\theta, L_{\mathbf{u}}\theta). \end{aligned} \tag{11}$$

Assuming that the initial condition of the signal generator $\theta(0)$ is such that $(L_{n_e}, L_{\mathbf{u}}, S, \theta(0))$ is minimal, and considering that the eigenvalues of $S$ are purely imaginary, there exists a mapping $\pi$, the *moment* of the tidal barrage system, which solves the following partial differential equation

$$\frac{\partial\pi(\theta)}{\partial\theta} S\theta = f(\pi(\theta), L_{n_e}\theta, L_{\mathbf{u}}\theta). \tag{12}$$

Furthermore, for any fixed trajectory $\theta(t)$, the steady-state response of the system can be computed in terms of its associated moment:

$$\begin{aligned} n_i^{ss}(t) &\approx \pi(\theta(t)) = L_{n_i}\theta(t), \\ \dot{n}_i^{ss}(t) &\approx L_{n_i}\dot{\theta}(t) = L_{n_i}S\theta(t), \end{aligned} \tag{13}$$

where $L_{n_i}^{\top} \in \mathbb{R}^{\nu}$ is the vector approximating the state of the system $n_i$ in the moment domain. As a result, the using the moment-based parameterisation, the continuous-time tidal barrage system is discretised as a linear combination of the harmonic functions given by $\mathcal{G}$:

$$\begin{aligned} \dot{\theta} &= S\theta, \\ n_o &\approx L_{n_e}\theta, \\ \mathbf{u} &= L_{\mathbf{u}}\theta, \\ n_i &\approx L_{n_i}\theta \end{aligned} \tag{14}$$

$L_{n_i}$ is computed by applying a Galerkin-like method [17] where a residual function $\mathcal{R}$ is forced to be 0 at a finite set of *time collocation points* $N_c \in \mathbb{N}$. $\mathcal{R}$ is defined by replacing the state and inputs in $f(n_i, n_e, \mathbf{u})$ (Eq. (7)) with their moment-based parameterisation:

$$\begin{aligned} \mathcal{R}(L_{n_i}, L_{n_e}, L_{\mathbf{u}}, t) = {} & A_b L_{n_i} S\theta(t) + L_{Q_t}\theta(t) \\ & + \text{sign}\left((L_{n_i} - L_{n_e})\theta(t)\right) C_{ds} L_{A_s}\theta(t)\sqrt{2g|L_{n_i} - L_{n_e}|\theta(t)}. \end{aligned} \tag{15}$$

Forcing $\mathcal{R}$ to be 0, at a set of $N_c$ collocation points, results in the following non-linear system of equations:

$$R(L_{n_i}, L_{n_e}, L_{\mathbf{u}}) = \begin{bmatrix} \mathcal{R}(L_{n_i}, L_{n_e}, L_{\mathbf{u}}, t_1) \\ \vdots \\ \mathcal{R}(L_{n_i}, L_{n_e}, L_{\mathbf{u}}, t_{N_c}) \end{bmatrix} = 0, \tag{16}$$

whereby $L_{n_i}$ can be computed, provided $N_c \geq \nu$.

### 3.2. Receding-horizon control

Receding-horizon control consists of iteratively solving the OCP over a time interval, and retrieving the optimal trajectories of the controlled variables for a shorter *control* period. The receding-horizon control strategy, implemented in this study, is summarised in the following algorithm, written in pseudo-code:

```
$N \leftarrow 1$ ;
while $N \leq N_{max}$ do
    Initialize $t_N$ (current time instant);
    Compute projection of tidal elevation $n_e \approx L_{n_e}^N \theta$;
    Compute optimal control solution $\mathbf{u}^{N,\text{opt}} = L_{\mathbf{u}}^{N,\text{opt}}\theta$;
    Retrieve $\mathbf{u}^{N,\text{opt}}$ for the interval $\Phi_c^N$;
    Update $t_N = t_N + T_c$;
    $N \leftarrow N + 1$;
end
```

First, at step $N$, the external input $n_e$, retrieved over an interval $\Phi^N$ of length $T_h$, *i.e.* the time horizon, is projected onto the signal generator $\mathcal{G}$, as detailed in Section 3.3. $\Phi^N$ is centred at the present time instant $t_N$, such that $\Phi^N = \Phi_p^N \cup \Phi_f^N$, where $\Phi_p^N = [t_N - \frac{T_h}{2}, t_N)$ is the past interval, $\Phi_f^N = [t_N, t_N + \frac{T_h}{2}]$ is the future interval. Using the moment-based control parameterisation, described in Section 3.1, the tidal barrage OCP at each step $N$ is formulated as follows:

$$L_{\mathbf{u}}^{N,\text{opt}} = \arg\max_{L_{\mathbf{u}}^N} \int_{\Phi^N} P(L_{n_i}^N, L_{n_e}^N, L_{\mathbf{u}}^N)\text{d}t,$$

subject to

$$\begin{aligned} & R(L_{n_i}^N, L_{n_e}^N, L_{\mathbf{u}}^N) = 0, \\ & L_{n_i}^N \mathcal{A} \leq \mathcal{B}_{n_i}, \\ & L_{\mathbf{u}}^N \mathcal{A} \leq \mathcal{B}_{\mathbf{u}}, \\ & \rho g \mu^N \odot (L_{n_i}^N - L_{n_o}^N)\Lambda \odot \left(L_{Q_t}^N \Lambda\right) \leq \mathcal{B}_{P_t}, \end{aligned} \tag{17}$$

where $\mu^N$ is the turbine efficiency, mapped in the moment-domain parameterisation (*i.e.*, as a function of $L_{n_i}^N$, $L_{n_e}^N$, and $L_{\mathbf{u}}^N$), $\odot$ denotes the standard element-wise (Hadamard) product, and

$$\begin{aligned} \Lambda &= \left[\theta(t_1) \; \dots \; \theta(t_{N_c})\right], \\ \mathcal{A} &= [\Lambda \;\; \Lambda], \\ \mathcal{B}_{n_i} &= \left[n_i^{\max}\mathbf{1}_{N_c} \;\; n_i^{\min}\mathbf{1}_{N_c}\right], \\ \mathcal{B}_{\mathbf{u}} &= \left[\mathbf{u}^{\max}\mathbf{1}_{N_c} \;\; \mathbf{u}^{\min}\mathbf{1}_{N_c}\right], \\ \mathcal{B}_{P_t} &= \left[P_t^{\max}\mathbf{1}_{N_c}\right]. \end{aligned} \tag{18}$$

Note that, in (17), the constraints are enforced at the set of $N_c$ collocation points. The control solution $L_{\mathbf{u}}^{N,\text{opt}}$ is then retrieved for the control period $\Phi_c^N = [t_N, t_N + T_c]$ of length $T_c < T_h$, the horizon is moved forward a period $T_c$, and the procedure is repeated.

Discontinuities between two consecutive control solutions are handled by overlapping the solution from step $N-1$ with the solution from step $N$, within an interval $\Phi_t^N = (t_{N-1}+T_c, t_{N-1}+T_c+T_t] = (t_N, t_N+T_t] \in \Phi_c^N$, of length $T_t \ll T_c$, and defining a smooth transition by means of a transition function [18], as depicted in Fig. 4. The resulting control solution, $\mathbf{u}_t^{N,\text{opt}}$ is calculated as:

$$\mathbf{u}_t^{N,\text{opt}} = \xi(-\mathbf{t})\, \mathbf{u}^{N-1,\text{opt}}\Big|_{\Phi_t^N} + \xi(\mathbf{t})\, \mathbf{u}^{N,\text{opt}}\Big|_{\Phi_t^N}, \tag{19}$$

with $\xi : \Phi_t^N \rightarrow [0, 1]$ a hyperbolic tangent function evaluated at $\mathbf{t} = t - T_t/2$, defined as:

$$\xi(\mathbf{t}) = \frac{\tanh(\mathbf{t}) + 1}{2}, \tag{20}$$

with $\xi(-\mathbf{t}) + \xi(\mathbf{t}) = 1 \forall t$.

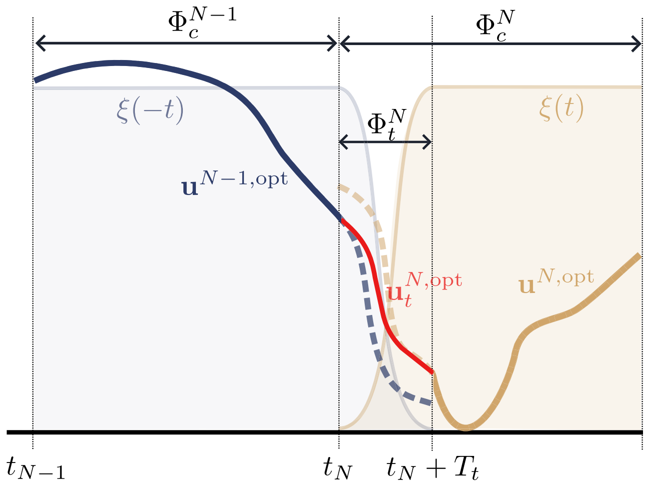

**Fig. 4.** Smooth transition between consecutive control actions at $\Phi_t^N$.

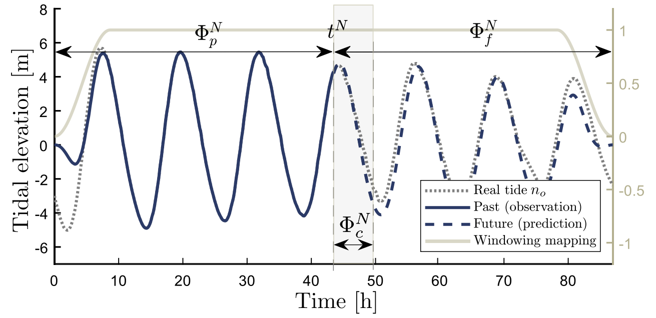

**Fig. 5.** Representation of the tidal elevation as input in each time horizon, using the observations at $t \in \Phi_p^N$ and predictions at $t \in \Phi_f^N$.

### 3.3. Input parameterisation

Because the OCP is solved for a time period $\Phi^N$, centred in the present instant $t_N$, the input $n_e$ can be represented using real observations, $n_e := n_o$, for all $t \in \Phi_p$, and a prediction, for all $t \in \Phi_f$, as seen in Fig. 5. This way, information about real tidal variations is included for $t \in \Phi_p$, and updated at each step of the receding-horizon algorithm. Additionally, the receding-horizon framework enables the use of a tidal elevation forecast for $t \in \Phi_f$, which can also be updated at each step.

To ensure that the OCP in the moment-based parameterisation is well posed, the inputs of the system must be periodic over the period $T_h$, used for the control calculations. To this end, at each step $N$ of the receding-horizon algorithm, $n_e$ is windowed onto a $T_h$−periodic mapping $\mathcal{L}^N : \Phi^N \rightarrow [1, 0]$, that smoothly drives $n_e$ to zero at the extremities (see Fig. 5, right axis). The windowed tidal elevation $n_e^{\mathcal{L}^N}$ is then projected onto the harmonic space given by the signal generator $\mathcal{G}$. As a result, the moment-based parameterisation of $n_e^{\mathcal{L}^N}$ at each step $N$ is defined as:

$$n_e \approx n_e^{\mathcal{L}^N} = \mathcal{L}^N n_e \approx L_{n_e}^N \theta. \tag{21}$$

Fig. 5 shows how, at the extremities of $\Phi^N$, the approximation of $n_e$ in the moment-domain is relatively poor, compared to the real tidal elevation, $n_o$, because of the windowing mapping used. On the other hand, at the centre of $\Phi^N$, the effect of $\mathcal{L}^N$ on the representation of $n_e$ is negligible. Therefore, the period $T_h$, chosen for the control calculations, influences how accurate the transcription of the problem is at $\Phi_c^N$ (for a fixed control length $T_c$), where the control solution is retrieved, and how much information is fed to the controller regarding the external input (similar to standard MPC methods). Furthermore, as mentioned in Section 3.1, the fundamental frequency of the signal generator $\mathcal{G}$, $\omega_o$, depends on the chosen $T_h$; the longer $T_h$ is, the higher de dimensionality of the moment-based parameterisation, for a fixed $\omega_{co}$, resulting in a more accurate representation of the system, with its associated higher computational cost.

**Table 2**
Data used to model the external input $n_e$ of the receding-horizon controller.

| Forecast | $n_e \forall t \in \Phi_p^N$ | $n_e \forall t \in \Phi_f^N$ |
|---|---|---|
| Observation | $n_o$ | $n_o$ |
| Astronomic | $n_o$ | $n_a$ |
| Weather-informed | $n_o$ | $n_f$ |

Fig. 6 shows a block diagram describing the receding-horizon moment-based controller pipeline. To model the external input $n_e$, at the prediction horizon $\Phi_f^N$, three cases are considered, summarised in Table 2:

- Using the observed tide $n_o$, extracted from tide gauge observations at St. Malo;
- Using the astronomic tide in St. Malo, $n_a$, from the EOT20 global tidal model (see Section 2.1);
- Using a weather-informed tidal forecast at St. Malo, $n_f$, published weekly in the EDF France website [19];

## 4. Results

This section presents the results obtained from solving the tidal barrage OCP, using the receding-horizon moment-based control framework, described in Section 3. The control time $T_c$, from which the control solution is retrieved at each step $N$ of the receding-horizon algorithm, is 1 h, with $N_{\max} = 720$, so that the simulation span is $\Omega = 1$ month, as pictured in Fig. 7. The control solutions are then combined, as described in Section 3.2, to create an optimal trajectory of $\mathbf{u}^{\text{opt}} = [Q_t^{\text{opt}}, A_s^{\text{opt}}]$ throughout the period $\Omega$, which is then implemented in the time domain, to calculate the steady state response of the system, $n_i$, and the generated energy, $E = \int_\Omega P_t \mathrm{d}t$.

### 4.1. Choice of control horizon length $T_h$

As a first step, the influence of the control horizon length $T_h$ on the controller performance is evaluated by computing optimal turbine flow and sluice gate area with different values of $T_h$. In this section, the ideal case is considered, where the observed tide $n_o$ is used to model both past (at $\Phi_p^N$) and future (at $\Phi_f^N$) tidal elevation. Fig. 8 shows, on the left axis, energy generation $E$, resulting from the optimal operation computed with each value of $T_h$; the dotted line marks $E = 97\%\, E_{\max}$, $E_{\max}$ being the maximum energy, achieved at $T_h = 26$ h, showing that, after $T_h = 24$ h, $E$ remains within a 3% margin. Note that the results shown in this section are specific for the control period selected, $T_c = 1$ h. The right axis in Fig. 8 shows the cumulative deviation of the state $n_i$ from the constraints $n_i^{\max}$ and $n_i^{\min}$, $\Delta_{n_i}$, computed as:

$$\Delta_{n_i} = \int_\Omega \max(n_i - n_i^{\max}, 0)\mathrm{d}t - \int_\Omega \min(n_i - n_i^{\min}, 0)\mathrm{d}t. \tag{22}$$

Since the moment-based parameterisation is an *approximation* of the system, it is expected that, when implementing the control solution (*i.e.* the optimal trajectories of $Q_t$ and $A_s$) in the time domain, the trajectory of the system state $n_i$ can deviate from the moment of the system $L_{n_i}^N \theta$, computed within the controller. This approximation error may propagate through subsequent steps of the receding-horizon algorithm, and cause the state $n_i$ to exceed the constraints. Larger values of $T_h$ enhance the approximation of the system in the moment-domain parameterisation at the centre of the period $T_h$, as described in Section 3.3, decreasing the difference between $n_i$ and $L_{n_i}^N \theta$, and,

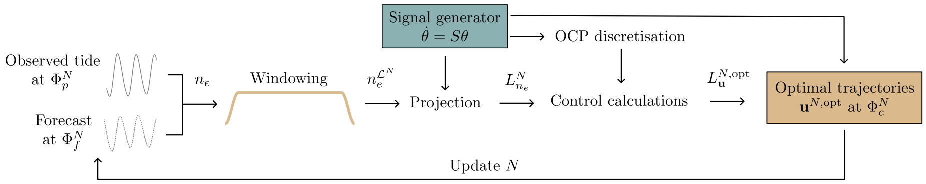

**Fig. 6.** Block diagram of the receding-horizon moment-based optimal controller.

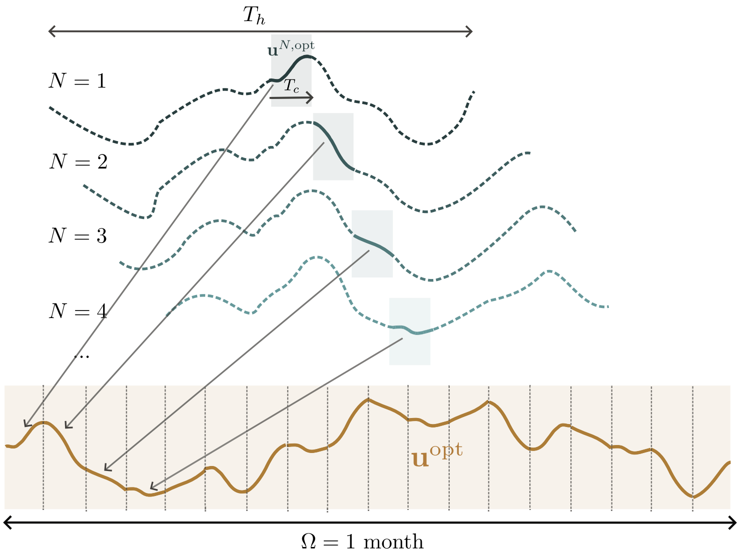

**Fig. 7.** Implementation of the receding-horizon algorithm: The optimal control solution $\mathbf{u}^{N,\text{opt}}$ is retrieved at each step $N$ for a period $T_c$, and the optimal trajectory $\mathbf{u}^{\text{opt}}$ for $\Omega = 1$ month is formed by combining all optimal solutions $\mathbf{u}^{N,\text{opt}}$ for $N = [1, 720]$.

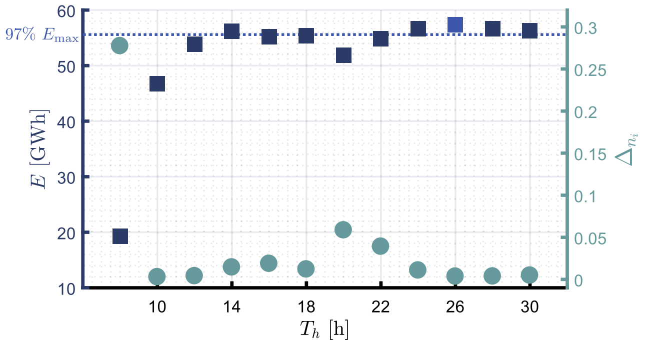

**Fig. 8.** Left axis: Energy $E$ generated using different horizon lengths $T_h$ (blue squares), and 3% margin from maximum energy (dotted line). Right axis: Cumulative constraint deviation in basin level, $\Delta_{n_i}$. (For interpretation of the references to colour in this figure legend, the reader is referred to the web version of this article.)

consequently, $\Delta_{n_i}$. Fig. 9 shows the moment-domain parameterisation of the state of the system, $L_{n_i}^N\theta$ (in black) for $N \in [1, N^{\max}]$, and time domain solution of the state of the system, $n_i$ (in green), obtained for different values of $T_h$, for a time snippet of 420 h. As $T_h$ increases, $n_i$ better resembles $L_{n_i}^N\theta$, and exceeds the constraints (represented by red dashed lines) less frequently.

$E$ is expected to increases with $T_h$; as seen in Section 3.3, the choice of $T_h$ defines how much (past and future) information about the tidal elevation is fed to the controller, as well as the solution space of the moment-based parameterisation of the OCP. However, Fig. 8 shows how $E$ does not increase monotonically with $T_h$. This can be attributed to the sensitivity of the control solution to the discretisation resulting from each value of $T_h$. The most dominant frequency, present in the tidal elevation at La Rance, is that corresponding to the astronomic constituent $M_2$, with a period of 12.42 h, and a frequency $\omega_{M_2} = 0.5059$ rad/h. Fig. 10 represents the solution space $\theta$ at each value of $T_h$, where each dot corresponds to a frequency, and each colour to a different $T_h$. For each solution space, a specific frequency has the minimum distance to $\omega_{M_2}$ (depicted with a red edge in Fig. 10), computed as the $\mathcal{L}^1$-norm of the difference between both frequencies:

$$d(\omega, \omega_{M_2}) = |\omega - \omega_{M_2}|. \tag{23}$$

The right axis in Fig. 10 shows how $d(\omega, \omega_{M_2})$ varies with $T_h$, resembling the behaviour of $E$ and $\Delta_{n_i}$ in Fig. 8. The distance $d(\omega, \omega_{M_2})$ is highest at $T_h = 8$ h, where $E$ is lowest, and $\Delta_{n_i}$ is highest. As $T_h$ increases, $d(\omega, \omega_{M_2})$ decreases, but with a relative increase between $T_h = 14$ h and $T_h = 22$ h; at those same values of $T_h$, there is a slight decrease in $E$ and increase in $\Delta_{n_i}$. After $T_h = 26$ h, $d(\omega, \omega_{M_2})$ increases again, but because of the higher number of frequencies in $\theta$, $E$ remains within the 3% margin of $E_{\max}$.

### 4.2. Using astronomic and weather-informed forecasts as prediction

In this section, the input $n_e$, used in the receding-horizon moment-based controller, combines observations $n_o$, at the past interval $\Phi_p^N$, and a forecast, at the future interval $\Phi_f^N$, for all $N \in [1, N^{\max}]$. The two forecasts considered are the astronomic tide $n_a$, and a weather-informed forecast $n_f$, as shown in Table 2.

Fig. 11 shows, in blue, the ideal case of using $n_o$ at $\Phi_f^N$, presented in Section 4.1, while the results from using $n_a$ and $n_f$ as forecasts are shown in green and yellow, respectively. Fig. 12 shows the percentage difference between the energy generated in the ideal case ($E^{n_o}$) and using $n_a$ as forecast ($E^{n_a}$), between the ideal case and using $n_f$ as forecast ($E^{n_f}$), and between $E^{n_f}$ and $E^{n_a}$. The difference between the ideal case and using $n_a$ (Fig. 12(a)), interpreted as the impact of storm

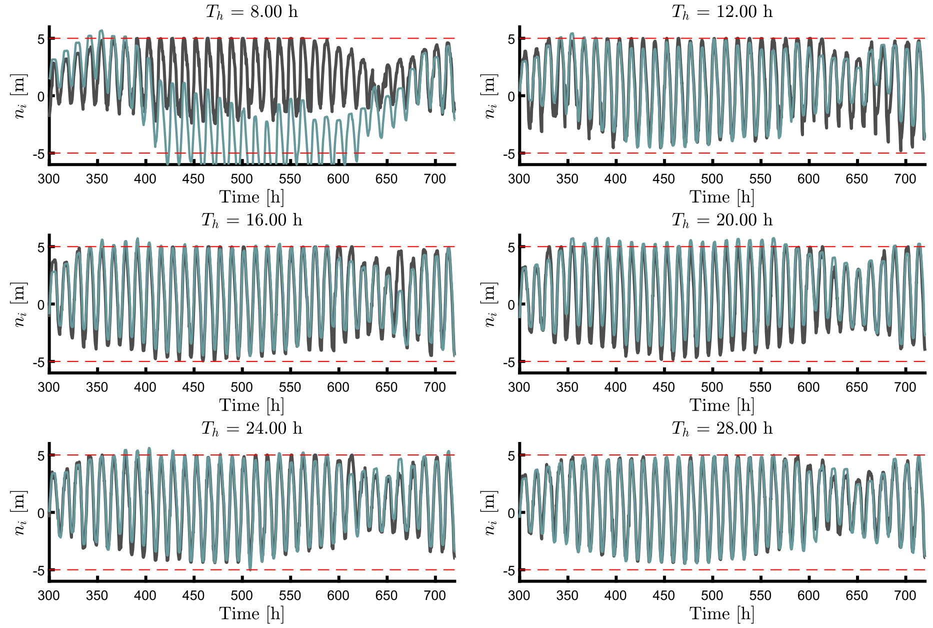

**Fig. 9.** Moment-domain parameterisation of the state of the system, $L_{ni}^{N}\theta$ (black line) for $N \in [1, N^{\max}]$, and time domain solution of the state of the system, $n_i$ (green line), for different values of $T_h$. The red dashed lines represent the constraints $n_i^{\max}$ and $n_i^{\min}$. (For interpretation of the references to colour in this figure legend, the reader is referred to the web version of this article.)

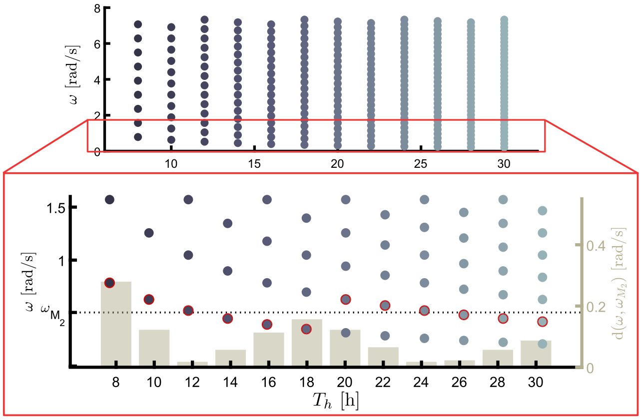

**Fig. 10.** Left axis: Solution space $\theta$ of the moment-based parameterisation of the tidal barrage system, for different values of $T_h$ (in different colours). Each dot represent a frequency, present in $\theta$; those dots with red edge are the frequencies closest to the frequency of the $M_2$ constituent, $\omega_{M_2}$. Right axis: Distance between the frequencies with red edge and $\omega_{M_2}$. (For interpretation of the references to colour in this figure legend, the reader is referred to the web version of this article.)

surge on the optimal control solution, is between 1.5% and 11.6%; On the other hand, using $n_f$ results in energy generation closer to the ideal case (Fig. 12(b)), compared with using $n_a$; the maximum energy achieved with $n_f$ is 1.4% below the maximum achieved in the ideal case, while the maximum energy achieved with $n_a$ as forecast is below 97% of the maximum achieved in the ideal case. The difference between the ideal case and using $n_f$, interpreted as the residual impact of forecast error on the optimal control solution, is below 5.4%, and almost negligible at $T_h = 30$ h. Note that, using either $n_a$ and $n_f$ as forecasts, the difference in energy compared to the ideal case tends to decrease with increasing $T_h$, and energy generation increases; in other words, the performance of the controller improves with increasing $T_h$, independently of the forecast used. Fig. 12(c) shows that using $n_f$ as prediction increases energy from 1% to 6% of the power plant

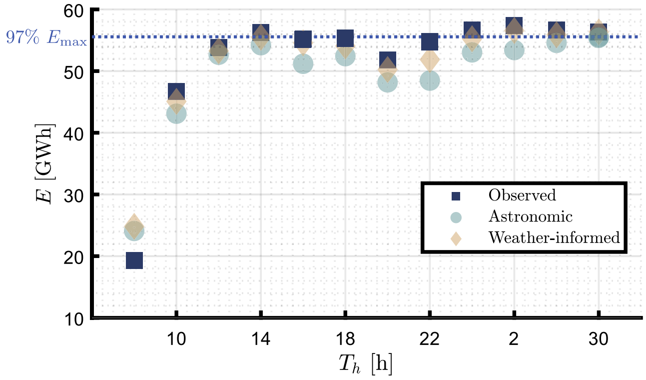

**Fig. 11.** Energy $E$ considering $n_o$, $n_a$ and $n_f$ to model the external input $n_e$ at $\Phi_f^N$ (Table 2), using different horizon lengths $T_h$. (For interpretation of the references to colour in this figure legend, the reader is referred to the web version of this article.)

capacity, compared to using $n_a$ as prediction. That is, in the study case considered, there is a net benefit in using the weather-informed forecast available.

Note that, as described in Section 2.1, the RMSE of $n_f$ compared to $n_o$ is 0.15 m, 1.2% of the maximum tidal range of 13 m, while the RMSE of $n_a$ is 0.35 m, 2.7% of the maximum tidal range. That is, the RMSE between $n_f$ and $n_o$ is 57% lower than the RMSE between $n_f$ and $n_o$. On the other hand, the gap between the maximum energy achieved with $n_f$ and $E_{\max}$ is 1.4%, 57% lower than the gap between the maximum energy achieved with $n_a$ and $E_{\max}$, which is 3.3%. As might be expected, if the available weather-informed forecast has a larger error, compared to $n_o$, than the astronomic tide, the performance of the controller may be inferior compared to simply ignoring storm surge. Therefore, the accuracy of $n_a$ as an approximation of $n_o$ should be used as a threshold to evaluate if the weather-informed forecast is adequate or not for the control calculations.

Fig. 13 shows the inner basin level $n_i$, computed in the time domain with the optimal control solutions from using observations as prediction

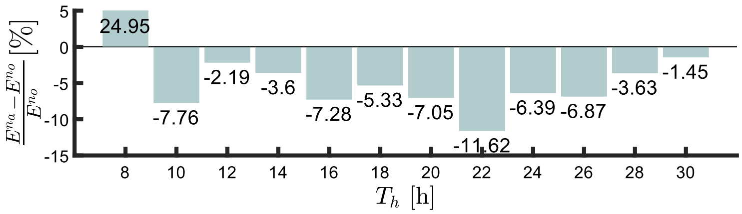

(a) Percentage difference in energy between using $n_o$ and $n_a$ at $\Phi_f^N$.

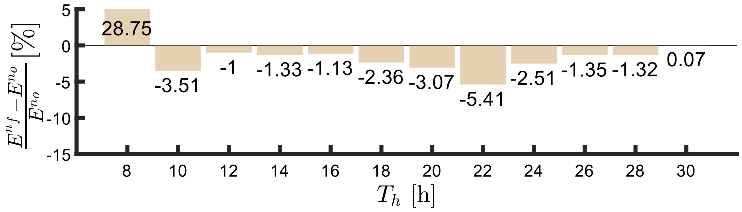

(b) Percentage difference in energy between using $n_o$ and $n_f$ at $\Phi_f^N$.

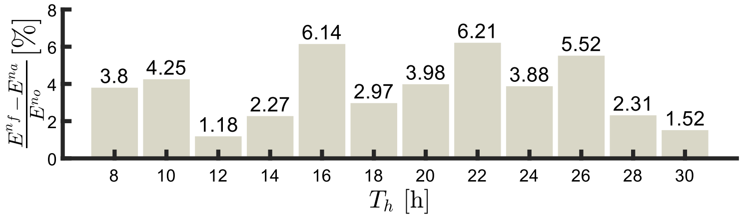

(c) Percentage difference in energy between using $n_f$ and $n_a$ at $\Phi_f^N$.

**Fig. 12.** Comparison in energy generated between the ideal case and using $n_a$ (a) and $n_f$ (b) as forecasts, and comparison in energy generated between using $n_a$ and $n_f$ as forecasts (c). $E^{n_o}$ is the energy generated using $n_o$ at $\Phi_f^N$, $E^{n_a}$ is the energy generated using $n_a$ at $\Phi_f^N$, and $E^{n_f}$ is the energy generated using $n_f$ at $\Phi_f^N$.

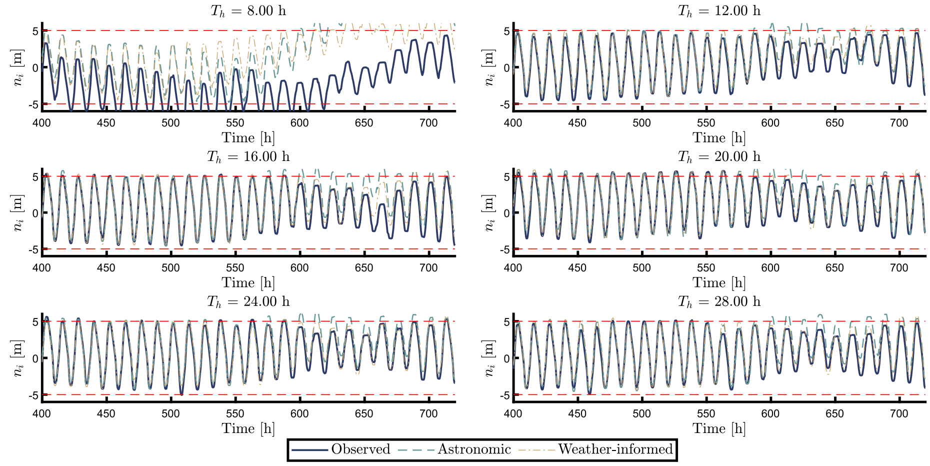

**Fig. 13.** Time domain solution of the state of the system, $n_i$, using observed tide $n_o$ (ideal case), astronomic tide $n_a$, and weather-informed forecast $n_f$ as prediction, for different values of $T_h$. The red dashed lines represent the constraints $n_i^{\max}$ and $n_i^{\min}$. (For interpretation of the references to colour in this figure legend, the reader is referred to the web version of this article.)

(solid blue line, as in Fig. 9), and from using either the astronomic tide $n_a$ (green line) and the weather-informed forecast $n_f$ (yellow line) as prediction. The solution, using the weather-informed forecast $n_f$, resembles more closely the ideal case, compared to the solution using only the astronomic tide $n_a$. To illustrate the improved performance of the controller when using $n_f$, note that, in Fig. 3(b), during neap (low) tides, at $t = 600$ h, the storm surge is relatively high; as a result, as shown in Fig. 13, the inner basin level $n_i$ is above the maximum constraint, for all values of $T_h$, when using $n_a$ as prediction, while using $n_f$ results in a control solution that maintains $n_i$ within the constraints.

Regarding the optimal trajectories of $\mathbf{u} = [Q_t, A_s]$, it is seen that the solutions $[Q_t^{n_f}, A_s^{n_f}]$, using $n_f$ as forecast, are closer to the solutions $[Q_t^{n_o}, A_s^{n_o}]$, from the using observations as forecast, in the least-square sense, compared to $[Q_t^{n_a}, A_s^{n_a}]$, obtained from using $n_a$ as forecast. Fig. 14 shows the RMSE between optimal solutions from the ideal case and each forecast; the lines represent the RMSE of the turbine flow $Q_t$ (left axis), while the squares represent the RMSE of the sluice gate area $A_s$

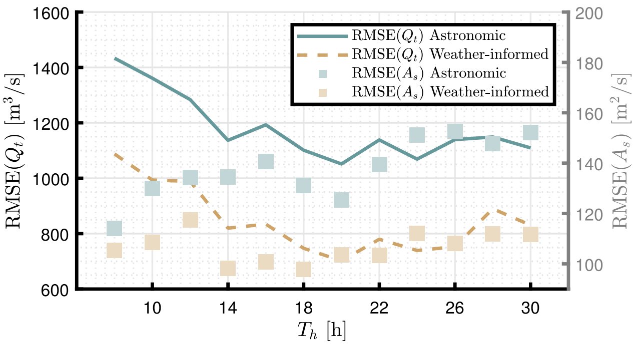

**Fig. 14.** Left axis: RMSE of the control solution $Q_t^{n_a}$ (using $n_a$ as forecast) with respect to the ideal control solution $Q_t^{n_o}$ (blue line), and RMSE of the control solution $Q_t^{n_f}$ (using $n_f$ as forecast) with respect to $Q_t^{n_o}$ (dashed yellow line). Right axis: RMSE of the control solution $A_s^{n_a}$ (using $n_a$ as forecast) with respect to the ideal control solution $A_s^{n_o}$ (blue squares), and RMSE of the control solution $A_s^{n_f}$ (using $n_f$ as forecast) with respect to $A_s^{n_o}$ (yellow squares). (For interpretation of the references to colour in this figure legend, the reader is referred to the web version of this article.)

(right axis), for different values of $T_h$. As expected, for every value of $T_h$, using $n_f$ as forecast, results in optimal control trajectories with lower RMSE, with respect to the optimal trajectories from the ideal case, than the trajectories obtained using $n_a$ as forecast.

### *4.3. Computational considerations and real-time implementation*

As described in Section 3, increasing the horizon $T_h$ reduces the fundamental frequency $\omega_o$; hence, for a fixed cutoff frequency $\omega_{co}$, the dimensions in the signal generator, associated with the moment-domain parameterisation, increase. Numerically, this increased number of frequencies translates into a larger number of optimisation variables, *i.e.* number of coefficients, $2\nu$, of the control vector $L_{\mathbf{u}}$ (each control vector $L_{Q_t}$ and $L_{A_s}$ has $\nu$ coefficients). Additionally, higher dimensionality requires more collocation points $N_c$ to solve the residual function (16). To comply with the real time implementation needs of the receding-horizon controller, the increased computational runtime should not exceed $T_c$, assumed here to be equal to 1 h.

In this study, simulations were performed in MATLAB®, using an active-set solver [20], with a timestep d$t$ = 1.2 min. The PC used has a 13th Gen Intel®Core™ i7-1365U processor with 16 GB of RAM. Table 3 shows, for varying $T_h$, the number of optimisation variables $2\nu$, number of time steps $N_t$ (*i.e.* $T_h$/d$t$), and the number of collocation points $N_c$, which is chosen to be approximately $2\nu$. Fig. 15 shows, for the different $T_h$ considered throughout this section, the mean and maximum runtime of the 720 iterations of the receding-horizon control for the three cases considered (using $n_o$, $n_a$ and $n_f$ as prediction). Simulation runtime is measured using the MATLAB®functions tic and toc. The mean simulation runtime, for all three cases, increases almost linearly with $T_h$, and is relatively low compared to $T_c$ even with $T_h$ = 30 h. The maximum runtime is always below 50 min, which is considered acceptable for real time implementation; however, if the weather-informed forecast is updated at each receding-horizon step, such low margin may be insufficient depending on the simulation time of the weather model used.

## 5. Extended results: Cardiff lagoon project, UK

With the purpose of showing the consistent value of the proposed control framework across various settings, this section presents a further case study in the Severn Estuary, in the UK, where the tidal range resource is one of the highest in the world [21]. Since both the tidal range resource and the storm surge are highly site specific, the aim here is to test the controller on a different location, and evaluate how general the previous results, obtained from the La Rance study case, are. The tidal barrage power plant, considered in this section, is based on the proposed Cardiff lagoon project, described in detail in [22]; the design parameters used to model the Cardiff lagoon are summarised in Table 4.

The distribution of storm surge in Cardiff, shown in Fig. 16, is between −1.5 m and 1.5 m. The observed tide $n_o$, astronomic tide $n_a$, and storm surge $n_s$, at the location of the proposed Cardiff lagoon, for the time period under study, are shown in Fig. 17. For the 720 h period considered here, the RMSE between $n_o$ and $n_a$ is 0.48 m, with a maximum tidal range of approximately 12 m, and a maximum absolute surge of 1.3 m, that is, around 11% of the tidal range (larger than the 8% seen in the data used for La Rance, in Section 2.1).

The tidal barrage OCP is solved with the same receding-horizon moment-based control framework, used in the La Rance case, with $T_c$ = 1 h, and the same range of values of $T_h$. Hence, the solution space, used in the moment-domain parameterisation, is the same for both the La Rance case and the Cardiff Lagoon case, at each value of $T_h$. As seen in Fig. 18, the ideal case, using the real observations $n_o$ at $\Phi_f^N$, yields considerably more energy, compared with using only the astronomic tide $n_a$ as prediction. For every $T_h$ considered, using $n_a$ as forecast, results in energy between 5% and 78% lower than the ideal case, and all energy values are below 93% of the maximum energy achieved in the ideal case. It is evident that, not only does the presence of storm surge affect the optimal control solution of the barrage, as seen in the case of La Rance, but that higher storm surge levels, relative to the tidal range, results in higher energy losses from using the astronomic tide alone as a forecast.

The study in [9] investigates the impact of storm surge on tidal range energy generation of different proposed projects across the west coast of the UK, including the Severn Estuary. The results from [9] show

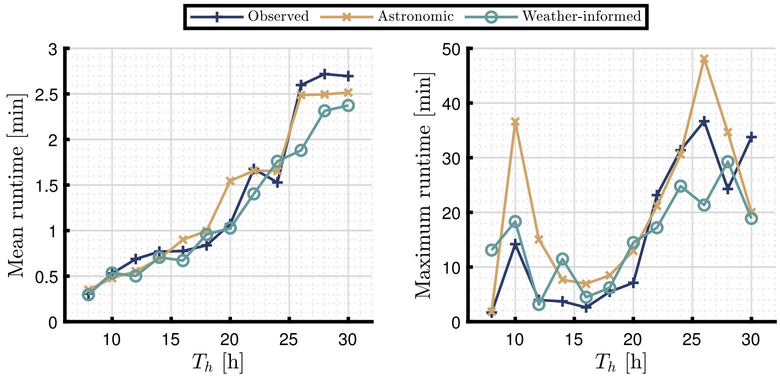

**Fig. 15.** Mean runtime (left plot) and maximum runtime (right plot) in minutes for different $T_h$, using $n_o$, $n_a$ and $n_f$.

**Table 3**
Simulation parameters for different $T_h$.

| $T_h$ [h] | 8 | 10 | 12 | 14 | 16 | 18 | 20 | 22 | 24 | 26 | 28 | 30 |
|---|---|---|---|---|---|---|---|---|---|---|---|---|
| $2\nu$ | 38 | 46 | 58 | 66 | 74 | 86 | 94 | 102 | 114 | 122 | 130 | 142 |
| $N_t$ | 401 | 501 | 601 | 701 | 801 | 901 | 1001 | 1101 | 1201 | 1301 | 1401 | 1501 |
| $N_c$ | 39 | 46 | 58 | 67 | 73 | 86 | 96 | 101 | 115 | 124 | 128 | 143 |

**Table 4**
Parameterisation of the Cardiff lagoon project, from [22].

| Parameter | Value | Unit |
|---|---|---|
| Maximum sluice gate area $A_s$ | 7200 | $m^2$ |
| Number of turbines $n_t$ | 98 | – |
| Turbines rated power | 20 | MW |
| Maximum turbine flow | 400 | $m^3/s$ |
| Sluice discharge coefficient $C_{ds}$ | 1 | – |

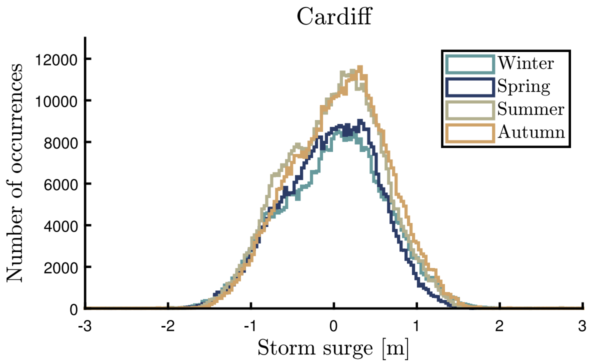

**Fig. 16.** Distribution of storm surge driven tidal level in St. Malo. *Source:* Data from 2020 to 2024.

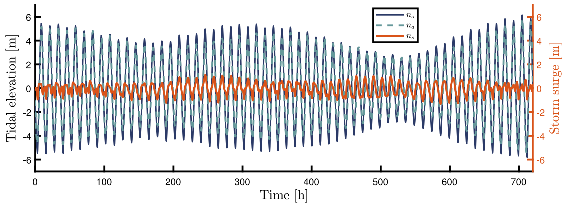

**Fig. 17.** Observed tidal elevation and astronomic tidal forecast, used as external inputs within the controller, and storm surge, at the location of the Cardiff lagoon.

that, with a fixed (not optimised) operational strategy, the simulated energy, generated using the astronomic tidal elevation as input, is up to 3% lower than the energy generated when including storm surge, for two-way generation, at lagoons located in the Severn Estuary. That is, the simulated impact of storm surge in energy generation is considerably lower than that seen in this section, where the proposed Cardiff lagoon generates, at best, 93% of the maximum energy achieved in the ideal case, when using the astronomic tidal elevation as prediction. However, the results from [9] are not comparable with this study, since no optimisation is involved in [9].

Moreover, Fig. 18 shows a relative decrease in energy for $T_h$ between 18 h and 24 h, similar to the case of La Rance (Fig. 8). In the Severn Estuary, as in St. Malo, the $M_2$ constituent is the most predominant constituent; hence, as explained in Section 4.1, the solution space $\theta$, when $T_h$ between 16 h and 22 h, poorly represents the system dynamics, because of the increased distance $d(\omega, \omega_{M_2})$ (Eq. (23)).

## 6. Conclusions

This paper presents a novel nonlinear receding-horizon moment-based control framework, whereby weather-driven tidal variations can be accounted for when addressing the tidal barrage OCP. It is seen that the horizon length $T_h$ influences the control solution significantly, due to its direct relation to the structure of the input and solution spaces in the moment domain. Given the predominance of the $M_2$ constituent in the tidal elevation, it is seen that the performance of the controller improves when the discretisation of the problem includes frequencies close to that corresponding to the $M_2$ constituent.

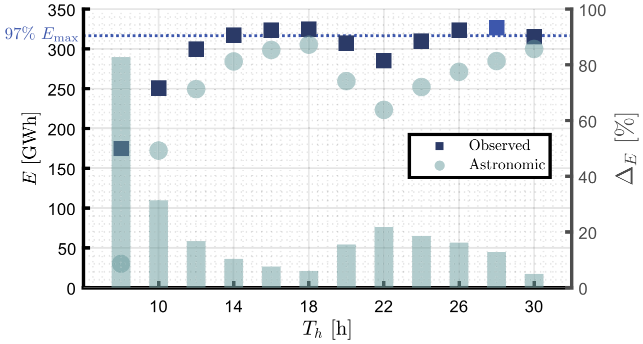

**Fig. 18.** Left axis: Energy $E$ considering $n_o$ and $n_a$ to model the external input $n_e$ at $\Phi_f^N$ in the case of the Cardiff lagoon, using different horizon lengths $T_h$. Right axis: Percentage difference in energy $\Delta_E$ between using $n_o$ and $n_a$ at $\Phi_f^N$.

Using only the astronomic tide as prediction, within the receding-horizon controller, yields lower energy generation, compared to the ideal case of having a perfect tidal elevation forecast. This suggests that, within the locations considered, although the tides are broadly considered as deterministic, storm surge has a non-negligible impact on the optimal control solution, and subsequent energy generation, for tidal barrages. Furthermore, the results show that there is an increase in energy generation, during the time period under study, when adding a forecast of the weather-driven tidal variations in the tidal elevation prediction, compared to using only the astronomic tidal elevation. These results emphasise the value of including, if available, a weather-informed forecast as input to the tidal barrage OCP, provided that the forecast is a better approximation (in the least-square sense) of the real tidal elevation than the astronomic tide. In this sense, the proposed control framework is suitable for online scheduling of tidal barrage operation, as it can effectively include real-time information of the tidal elevation, as well as an updated weather-informed storm surge forecast. The receding-horizon approach enables flexible scheduling of tidal barrages, whereby operation can be adapted throughout the day according to variable, and often unpredictable, weather conditions. Furthermore, optimal barrage operation can be efficiently computed using the moment-based control framework, enabling an hourly update of the control solution.

One of the limitations of this study is that the weather-driven tidal forecast used is not updated at each iteration of the receding-horizon controller. In general, the goodness of fit of weather forecasts decrease over time, which may lead to decreased controller performance when increasing $T_h$. Further research is needed to analyse the results when using periodically updated forecasts, which is not implemented in this study.

## CRediT authorship contribution statement

**Agustina Skiarski:** Writing – original draft, Visualization, Methodology, Investigation, Formal analysis, Data curation, Conceptualization.

**Nicolás Faedo:** Writing – review & editing, Supervision, Formal analysis. **John V. Ringwood:** Writing – review & editing, Supervision, Conceptualization.

## Declaration of competing interest

The authors declare that they have no known competing financial interests or personal relationships that could have appeared to influence the work reported in this paper.

## Acknowledgements

Agustina Skiarski is grateful for support of Taighde Éireann – Research Ireland under Grant number 18/CRT/6049. For the purpose of Open Access, the author has applied a CC BY public copyright licence to any Author Accepted Manuscript version arising from this submission. John Ringwood was supported by Science Foundation Ireland (SFI) through the MaREI Centre for Energy, Climate and Marine under Grant No. 12/RC/2302_P2.

## Data availability

Data will be made available on request.

## References

[1] Burrows R, Walkington I, Yates N, Hedges T, Chen D, Li M, Zhou J, Wolf J, Proctor R, Holt J, Prandle D. Tapping the tidal power potential of the Eastern Irish Sea. Technical report, Final report, joule project JIRP106/03, University of Liverpool and National Oceanography; 2009.

[2] Parker BB. Tidal analysis and prediction. NOAA special publication NOS CO-OPS, U.S. Department of Commerce, National Oceanic and Atmospheric Administration, National Ocean Service, Center for Operational Oceanographic Products and Services; 2007.

[3] Shen Y, Nyman P-O. Optimal operation of tidal plants based on nonlinear model predictive control strategy. IOP Conf Ser: Earth Environ Sci 2021;687(1):012101.

[4] Harcourt F, Angeloudis A, Piggott MD. Utilising the flexible generation potential of tidal range power plants to optimise economic value. Appl Energy 2019;237:873–84.

[5] Xue J, Ahmadian R, Jones O, Falconer RA. Design of tidal range energy generation schemes using a Genetic Algorithm model. Appl Energy 2021;286:116506.

[6] Skiarski A, Faedo N, Ringwood JV. Modelling and optimal control of tidal barrages: A moment-based approach. Renew Energy 2026;256:124632.

[7] Faedo N, Peña-Sanchez Y, Ringwood JV. Receding-horizon energy-maximising optimal control of wave energy systems based on moments. IEEE Trans Sustain Energy 2020;12(1):378–86.

[8] Skiarski A, Faedo N, Ringwood JV. Optimisation and control of tidal range power plants operation: Is there scope for further improvement? Energy Convers Manag: X 2024;23:100657.

[9] Lewis M, Angeloudis A, Robins P, Evans P, Neill S. Influence of storm surge on tidal range energy. Energy 2017;122:25–36.

[10] Moreira TM, de Faria JG, de Melo POV, Medeiros-Ribeiro G. Development and validation of an AI-Driven model for the La Rance tidal barrage: A generalisable case study. Appl Energy 2023;332:120506.

[11] Flanders Marine Institute (VLIZ). Sea level station monitoring facility. Technical report, Intergovernmental Oceanographic Commission (IOC); 2024, URL http://www.ioc-sealevelmonitoring.org. [Accessed October 2024].

[12] Hart-Davis MG, Piccioni G, Dettmering D, Schwatke C, Passaro M, Seitz F. EOT20: a global ocean tide model from multi-mission satellite altimetry. Earth Syst Sci Data 2021;13(8):3869–84.

[13] Charlier RH. Forty candles for the Rance River TPP tides provide renewable and sustainable power generation. Renew Sustain Energy Rev 2007;11(9):2032–57. http://dx.doi.org/10.1016/j.rser.2006.03.015.

[14] Angeloudis A, Piggott M, Kramer S, Avdis A, Coles D, Christou M. Comparison of 0-D, 1-D and 2-D model capabilities for tidal range energy resource assessments. In: Proceedings of the twelfth European wave and tidal energy conference. Cork, Ireland; 2017.

[15] Faedo. N, Scarciotti. G, Astolfi. A, Ringwood JV. Nonlinear energy-maximizing optimal control of wave energy systems: A moment-based approach. IEEE Trans Control Syst Technol 2021;29(6):2533–47.

[16] Ringwood JV, Faedo N. Tidal barrage operational optimisation using wave energy control techniques. In: Proceedings of the 14th IFAC conference on control applications in marine systems, robotics, and vehicles CAMS 2022. Vol. 55, Lyngby, Denmark: Elsevier BV; 2022, p. 148–53.

[17] Faedo N, Scarciotti G, Astolfi A, Ringwood JV. On the approximation of moments for nonlinear systems. Technical Report 11, 2021.

[18] Mérigaud A, Ringwood JV. Towards realistic non-linear receding-horizon spectral control of wave energy converters. Control Eng Pract 2018;81:145–61.

[19] EDF France. Marées en Rance. 2024, https://www.edf.fr/usine-maremotrice-rance/marees-en-rance.

[20] Gill PE, Murray W, Wright MH. Practical optimization. Academic Press; 1981.

[21] Neill SP, Angeloudis A, Robins PE, Walkington I, Ward SL, Masters I, Lewis MJ, Piano M, Avdis A, Piggott MD, Aggidis G, Evans P, Adcock TA, Židonis A, Ahmadian R, Falconer R. Tidal range energy resource and optimization – Past perspectives and future challenges. Renew Energy 2018;127:763–78. http://dx.doi.org/10.1016/j.renene.2018.05.007.

[22] Angeloudis A, Kramer SC, Hawkins N, Piggott MD. On the potential of linked-basin tidal power plants: An operational and coastal modelling assessment. Renew Energy 2020;155:876–88. http://dx.doi.org/10.1016/j.renene.2020.03.167.